Analytica Chimica Acta 1208 (2022) 339851

Contents lists available at ScienceDirect

Analytica Chimica Acta

journal homepage: www.elsevier.com/locate/aca

Lactate biosensing based on covalent immobilization of lactate oxidase onto chevron-like graphene nanoribbons via diazotization-coupling reaction

Raquel Sainz [a], María del Pozo [a], Luis Vázquez [b], Manuel Vilas-Varela [c], Jesús Castro-Esteban [c], Elías Blanco [a], María Dolores Petit-Domínguez [a], Carmen Quintana [a], Elena Casero [a,*]

[a] Departamento de Química Analítica y Análisis Instrumental, Facultad de Ciencias, c/ Francisco Tomás y Valiente, Nº7. Campus de Excelencia de la Universidad Autónoma de Madrid, 28049, Madrid, Spain
[b] Instituto de Ciencia de Materiales de Madrid (CSIC), c/ Sor Juana Inés de la Cruz Nº3. Campus de Excelencia de la Universidad Autónoma de Madrid, 28049, Madrid, Spain
[c] Centro Singular de Investigación en Química Biolóxica e Materiais Moleculares (CIQUS) and Departamento de Química Orgánica, Universidade de Santiago de Compostela, 15782, Santiago de Compostela, Spain

HIGHLIGHTS

- Synthesis of Chevron-like graphene nanoribbons by solution-based procedure (GNR).
- GNR as platform for covalent anchoring of lactate oxidase (LOx) via diazotation.
- GNR led to improved electrochemical biosensors for lactate determination.
- LOx affords selectivity & GNR together with covalent enzyme immobilization sensitivity.

GRAPHICAL ABSTRACT

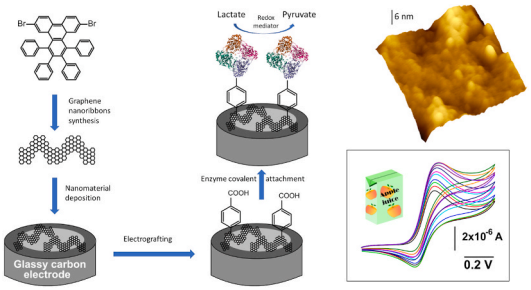

ARTICLE INFO

Keywords:
Biosensor
Chevron-like graphene nanoribbons
Lactate oxidase
Diazonium chemistry
Electrochemical detection
Lactate

ABSTRACT

We have designed and prepared an electrochemical biosensor for lactate determination. Through a diazotation process, the enzyme lactate oxidase (LOx) is anchored onto chevron-like graphene nanoribbons (GNR), previously synthesized by a solution-based chemical route, and used as modifiers of glassy carbon electrodes. In a first step, we have performed the grafting of a 4-carboxyphenyl film, by electrochemical reduction of the corresponding 4-carboxyphenyl diazonium salt, on the GNR-modified electrode surface. In this way, the carboxylic groups are exposed to the solution, enabling the covalent immobilization of the enzyme through the formation of an amide bond between these carboxylic groups and the amine groups of the enzyme. The biosensor design was optimized through the morphological and electrochemical characterization of each construction step by atomic force microscopy, scanning electron microscopy, cyclic voltammetry and electrochemical impedance spectroscopy.The cyclic voltammetric response of the biosensor in a solution of hydroxymethylferrocene in presence of L-lactate evidenced a clear electrocatalytic effect powered by the specific design of the biosensing platform with LOx covalently attached to the GNR layer. From the calibration procedures employed for L-lactate determination, a linear concentration range of $3.4 \cdot 10^{-5}$– $2.8 \cdot 10^{-4}$ M and a detection limit of 11 μM were obtained, with relative errors and relative standard deviations less than 6.0% and 8.4%, respectively. The applicability of the

* Corresponding author.
E-mail address: elena.casero@uam.es (E. Casero).

https://doi.org/10.1016/j.aca.2022.339851
Received 3 February 2022; Received in revised form 5 April 2022; Accepted 16 April 2022
Available online 20 April 2022
0003-2670/© 2022 The Authors. Published by Elsevier B.V. This is an open access article under the CC BY-NC-ND license (http://creativecommons.org/licenses/by-nc-nd/4.0/).

biosensor was tested by determining lactate in apple juices, leading to results that are in good agreement with those obtained with a well-established enzymatic spectrophotometric assay kit.

1. Introduction

The scientific community must try to improve the life quality of the citizens, who, due to changes in the way of life, demand foods and beverages ready-to-eat, fresh-like and with high nutritional value and flavour. Lactic acid-fermented foods (dairy products, meats, vegetables, and fish products) are known from ancient times and have been naturally produced by the microflora present in the raw material [1]. Nowadays, lactic acid bacteria (LAB) are also used in some fermented foods and are responsible for advantages at different levels: food preservation/safety (reduction of toxic and antinutritive compounds and production of antifungal compounds), nutritional (reduction of sugars, production of bioactive peptides, short chain fatty acids or polysaccharides), organoleptic (texture and aroma) and technological factors. In particular, the use of LAB to ferment items such as vegetables and fruits is a trend leading to produce fashionable products such as smoothies [2], because these products are better sold by the industry when their consumption is associated with health benefits.

In the processes where LAB are implicated, there is a logical production of lactic acid and the chemical profile of the above detrimental and beneficial compounds changes accordingly. So, the amount of lactic acid is related to the concentration of both healthy chemicals and toxic molecules present in fruits and vegetables [1–3].

In the food industry, for lactic acid determination, electrochemical enzyme-based biosensors represent an interesting alternative to other methodologies, as it is evidenced by recent publications [4–10], since they combine high sensitivity and selectivity provided by the electrochemical detection and the biological recognition element, respectively. In addition, the electrochemical methods have attracted attention because they offer low-cost equipment with a high easy-of-use, which are miniaturized and portable [11,12]. In this field, the development of biosensors based on low dimensional materials has attracted great interest as a way to improve the performance towards the analysis of the target [13]. Integration of nanomaterials and proteins leads to enhanced analytical characteristics, such as sensitivity, reproducibility and stability, as a consequence of a synergistic effect between them. Proteins recognize the target providing selectivity while nanomaterials facilitate the events from analyte recognition to signal generation due to their unique characteristics. Among them, their high surface area assists the load of the protein by providing a high number of immobilization sites, whereas their biocompatibility benefits the preservation of the enzyme catalytic activity and the nanomaterial structure can exert a protective effect against denaturation of the enzyme due to the external medium, thus enhancing the stability and reproducibility [14]. Accordingly, nanomaterials such as silver, gold, manganese dioxide or diamond nanoparticles, as well as other carbon-based nanomaterials, have been integrated with proteins, such as antibodies and enzymes, and widely employed for biosensing [15]. In particular, among the carbon-based nanomaterials, the isolation and characterization of graphene almost two decades ago have opened up a wide range of nanomaterials with excellent tuneable properties. Graphene nanoribbons consist of relatively narrow strips of sp^2 carbon atoms. Their width and structure at the edges alter the observed band gaps. Graphene sheets or carbon nanotubes are some of the precursors to obtain nanoribbons by top-down methodologies while the assembling of molecular building blocks, either on-surface or solution-based, is the basis of bottom-up procedures [16]. The latter have attracted a great attention since they provide uniform and highly defined structures, in contrast with the top-down strategies that lead to rather undefined and randomly shaped nanoribbons. Knowledge fields where nanoribbons are being applied are Li-ion batteries [17], energy storage [18], sensing [16], heavy metal decontamination [19], and fuel cells [20]. In the particular field of enzymatic biosensors, the employment of GNR as nanomaterial for improving the performance has not been widely explored, yet, as evidenced by the low number of works published since 2015 [21]. There are few reports and most of them are devoted to the determination of glucose. Furthermore, they require the employment of GNR in conjunction with other nanomaterials such as silver nanoparticles, manganese dioxide nanoparticles or carbon nanotubes [22–27]. However, since GNR have a higher number of open-ended structures than carbon nanotubes and graphene, leading to a large surface area and a high density of reaction edges, their use can help to the immobilization of the enzyme.

The development of GNR-based enzymatic biosensors involves the functionalization of the GNR with the enzyme, which can be achieved by a direct adsorption procedure or by covalent attachment. Procedures based on direct adsorption can be problematic since the enzyme is weakly bound to the surface and, therefore, they are usually less effective due to the lack of stability and reproducibility of the modification. In contrast, the chemical modification of GNR, involving functional groups covalently attached, can be a more adequate alternative. In this case, the covalent approach requires the incorporation of compounds with carboxylic groups on the GNR that allow a covalent bond with the amine groups of the enzyme. A well-established route for functionalization of carbon nanomaterials consists in the employment of aryl diazonium salts with different functional groups, such as electron withdrawing or electron donating groups [18,28–30]. Since its first application 20 years ago, this strategy remains active and its significance for biosensing applications is undoubtedly recognized [31]. The functionalization of carbon nanomaterials allows tailoring the interface properties and facilitates the immobilization of the biorecognition element. The most common mechanism involves the formation from diazonium compounds, after taking an electron from the carbon network and releasing of nitrogen gas, of an aryl radical that is subsequently incorporated to the lattice [28]. Azo-coupling has been used to modify nanostructures such as graphene, carbon nanotubes and, even, the transformation of the relative inert transition metal dichalcogenides has been recently achieved [32]. Among the advantages of the use of diazonium salts, it is worth mentioning the covalent bonding, the speed of the reaction, and the simplicity of the method [33]. To the best of our knowledge, there is no work in which the grafting of graphene nanoribbons has been explored.

Considering together the last mentioned facts, we present the development of a biosensor for lactic acid determination based on the covalent immobilization of the enzyme lactate oxidase onto a bottom-up synthesized graphene nanoribbons-modified glassy carbon electrode. GNR were functionalized via diazonium chemistry with a molecule containing a carboxylic group that forms an amide bond with the amine groups of the enzyme. The fabrication steps of the biosensor were electrochemically and morphologically characterized by cyclic voltammetry (CV), electrochemical impedance spectroscopy (EIS), scanning electron microscopy (SEM) and atomic force microscopy (AFM) techniques. The applicability of the biosensing platform in real sample analysis is evaluated by analyzing lactate in apple juices.

2. Experimental

2.1. Reagents

Hydroxymethyl ferrocene (HMF), N-(3-dimethylaminopropyl)-N′-ethylcarbodiimide hydrochloride (EDC), N-hydroxysuccinimide (NHS), *N*-methyl pyrrolidone (NMP), 4-aminobenzoic acid, sodium nitrite, L-

(+)-lactic acid lithium salt 97% and lactate oxidase (LOx) lyophilized powder (source *Aerococcus viridans*) containing 39 units/mg solid, were purchased from Merck (Darmstad, Germany). Lactate oxidase stock solutions were prepared dissolving 2.6 mg of the LOx lyophilized powder in 500 μL of 0.1 M phosphate buffer pH 7.0, aliquoted (10 μL) and stored at −30 °C. A commercial kit for lactate determination based on photometric measurements was purchased from Neogen (Lansing, Michigan, USA). For the solution-based synthesis of GNR, phenanthrene-9,10-quinone, 1,3-diphenylacetone, N-bromosuccinimide (NBS), diphenylacetylene, bis(1,5-cyclooctadiene)nickel(0) ($Ni(COD)_2$) and iron trichloride were also purchased from Merck (Darmstad, Germany). Phosphoric acid was supplied by Scharlab S.A. (Sentmenat, Barcelona, Spain) and employed for preparation of 0.1 M phosphate buffer. Ultrapure water was obtained by a Milli-Q™ system of Merck Millipore (Darmstad, Germany).

2.2. Instrumentation and materials

Cyclic voltammetric and electrochemical impedance spectroscopic measurements were carried out using an Autolab PGSTAT 302 N with GPES software from Metrohm Autolab (Utrecht, Netherlands) equipped with a Frequency Response Analyzer (FRAII). A Ag/AgCl (1.0 M KCl), as a reference electrode, a platinum wire, as a counter electrode, and a modified glassy carbon electrode (GC, geometric area of 7.07 mm^2), as working electrode were employed for electrochemical measurements. All solutions were deaerated with nitrogen gas before measurements.

The AFM characterization was performed with two systems: a Nanoscope IIIa from Veeco (Plainview, New York, United States) for the topographical and force curve analysis and a PicoPlus from Agilent (Santa Clara, California, USA) for the single pass Kelvin Force Microscopy (KFM) measurements under nitrogen atmosphere. For the former, silicon cantilevers (Veeco) with a nominal radius of curvature of 8 nm were used with two different nominal constant forces, namely 40 N/m and 1–5 N/m, the latter being used for the LOx-containing samples. Due to the unavoidable presence of large and rough aggregates (see below) the imaging conditions required the employ of relatively high free oscillation amplitudes (A_0) and setpoints of $0.8xA_0$ to $0.9xA_0$. For the electrical measurements, Pt coated tips, model ANSCM-PT-20, from AppNano (Mountain View, California, USA) with a radius smaller than 40 nm were employed. From the single pass KFM measurements two types of images can be obtained: an image where the signal is the Contact Potential Difference (CPD), whose changes are related to changes in the surface potential, and other image where the signal is proportional to the gradient of the tip-sample capacitance ($\partial C/\partial z$). Relative changes in this signal can be related to differences in the local dielectric constant [34]. In all these measurements, it was necessary to address carefully the tip to a given region on the sample surface, using the attached optical microscope, to avoid the large GNR structures.

SEM images were obtained with a NOVA NANOSEM 230 equipment from FEI (Hillsboro, Oregon, USA) operating with a low-voltage and high contrast detector (vCD). The landing electron beam energy was 6–7 keV.

2.3. Procedures

2.3.1. Synthesis of graphene nanoribbons

The synthesis of chevron-like GNR was performed following a previously reported procedure [35]. Monomer was obtained from phenanthrene-9,10-quinone in three steps, including bromination with NBS, condensation with 1,3-diphenylacetone, and reaction with diphenylacetylene. Then, $Ni(COD)_2$-promoted polymerization of the monomer followed by $FeCl_3$-promoted cyclodehydrogenation led to chevron-like GNR (Fig. 1). NMP was employed as solvent for preparing the graphene nanoribbons suspension (0.5 mg mL^{-1}). The suspension was obtained by treating the mixture with an ultrasonic probe (amplitude of 70%) for 2 min.

2.3.2. Preparation of the electrochemical biosensor platform

GC electrodes were polished with alumina powder (0.3 μm), sonicated in water/ethanol for 3 min and dried with N_2. The GC surface was modified by deposition of 5 μL of GNR and dried at 70 °C in an oven during 2 h (system denoted as GC/GNR). The electrografting modification of this surface was carried out by 4-aminobenzoic acid diazonium salt formed in situ by diazotization of 4-aminobenzoic acid solution (1 mM) in 0.5 M HCl at 4 °C, adding 0.5 mL of $NaNO_2$ solution (2 mM) under N_2 atmosphere and leaving the reaction to proceed for 5 min. After this time, the electrochemical reduction was carried out by performing 5 cyclic voltammetric scans from +0.6 V to −0.6 V (system denoted as GC/GNR/BzA). Once the grafting was complete, the carboxylic group activation for enzyme bonding was achieved by adding

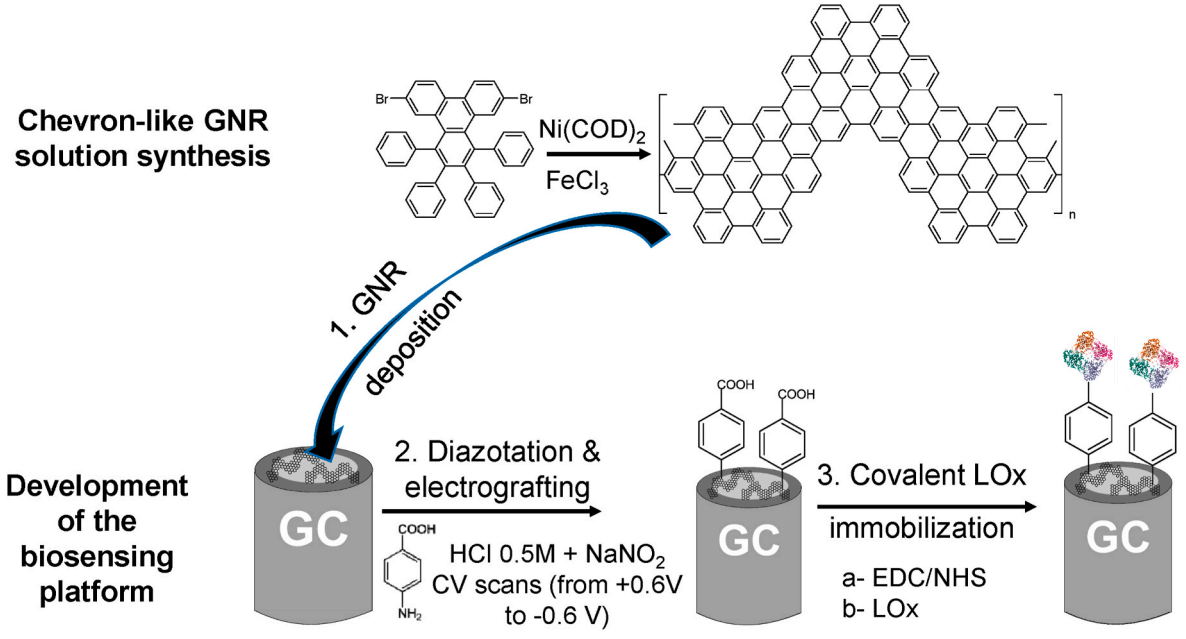

Fig. 1. Solution synthesis of chevron-like GNR and preparation of the lactate oxidase-based biosensor.

10 μL of a solution mixture containing 200 mM of N-(3-dimethylaminopropyl)-N′-ethylcarbodiimide hydrochloride (EDC) and 47 mM N-hydroxysuccinimide (NHS) onto the GC/GNR/BzA surface. After rinsing with water, 6 μL of lactate oxidase were dropped on the electrode surface and left them to dry at room temperature (system denoted as GC/GNR/BzA/LOx). The electrodes were kept at 4 °C until their use. Biosensor platforms with the enzyme immobilized by direct adsorption, instead of by a covalent approach, were also prepared. In this case, after the grafting process, 6 μL of lactate oxidase were dropped on the surface and left them to dry (without carrying out the activation of the carboxylic group of the benzoic acid with EDC and NHS). This system was denoted as GC/GNR/BzA/Lox_{ads}.

2.3.3. Preparation of the samples for AFM and SEM measurements

Samples for AFM and SEM measurements were prepared on glassy carbon rods in the same way described in the previous section for the electrochemical biosensors. In other previous AFM measurements on a similar system [16], we employed silicon as a substrate instead of GC, because GC is rougher and poorer in reflecting. In contrast, the flatness and high reflectance of silicon allowed us to locate the flat and terraced GNR aggregates. In this work, we have adopted a different approach since we have chosen to study the real system. This choice poses some practical problems because we are then unable to address the tip towards a flat and terraced GNR aggregate. Rather, we had to address the tip towards a zone free of large aggregates but this does not guarantee that some smaller tridimensional aggregates are present and, consequently, can alter the tip status when found during the tip scanning process. Notwithstanding, good quality topographical images of isolated and small GNR flakes have been taken although they did not show the neat terraced morphology found on those imaged on the silicon substrate [16]. Likewise, good quality KFM images have been obtained. It should be noted that the different wettability of NMP on GC with respect to that of silicon substrates can also influence the size and degree of aggregation of the GNR structures found on the surface. In fact, the NMP drop containing the GNR flakes is spread much better on GC than in silicon, which implies that is more probable to find smaller GNR flakes on the GC surface, as it is the case.

2.3.4. Lactate determination in apple juice samples by a standard addition procedure

An aliquot of apple juice from a local market (Madrid, Spain) was filtered through 0.45 μm syringe filter and analysed by a standard addition procedure. The employed procedure is as follows: i) several solutions were prepared by mixing an aliquot of 250 μL of the filtered apple juice with increasing amounts of a standard containing a known concentration of lactate and made up to 5.00 mL in volumetric flasks with 0.1 M phosphate buffer containing 1 mM of HMF, ii) the electrochemical responses of the GCE/GNR/BzA/LOx biosensor towards the as-prepared solutions were recorded.

3. Results and discussion

3.1. Construction and characterization of the biosensing platform

The development of the biosensor involves several steps, summarized in Fig. 1, where the GNR synthesis is also shown.

The procedure includes: i) the modification of the transductor, a GC electrode, with chevron-like graphene nanoribbons that have been synthesized through a solution-based chemical approach, ii) the formation of an aryl diazonium layer that exposes carboxylic groups to the outside and iii) the covalent immobilization of the biological element, lactate oxidase, to the device. The surface resulting after each building step has been characterized by AFM, and/or SEM and EIS.

3.1.1. Modification of GCE with GNR

First, we have studied by AFM the surface of the polished GC, which displays a series of grooves, around 30 nm deep, and widths in the 150–400 nm range (data not shown). These grooves are the consequence of the initial polishing and many of them run along parallel directions. At short length scales, a small granular structure is observed. As mentioned above, even given the practical problems for AFM imaging derived from the rough and poor reflecting character of the GC surfaces, we have preferred to carry out the measurements employing this substrate instead of the usually employed in AFM (mica, silicon or highly oriented pyrolytic graphite) in order to study the real system. Over this GC surface, GNR were deposited. As commented before, GNR were synthesized using a solution-based chemical approach that, in comparison with on-surface synthesis procedures, yields bulky amounts of GNR, allowing their deposition on different substrates. In contrast with top-down methodologies, in particular those based on unzipping of carbon nanotubes, the solution-based synthesis also leads to more structurally well-defined and homogenous GNR. However, this type of GNR has been scarcely employed for developing biosensing platforms.

Fig. 2a shows a SEM micrograph obtained on a GC surface modified with GNR. In this image, different aggregates are observed with a large range of lateral sizes, from the submicron scale up to 4–5 μm wide.

The morphology of the aggregates can be either quite rough or flat at the SEM scale. Precisely, Fig. 2b depicts a detail of one of these flat aggregates. The dispersion in sizes and morphologies of the GNR deposits turns the AFM characterization into a complex task since the large or even submicron aggregates are indeed quite rough for the AFM technique and their imaging can damage the tip condition irreversibly. One of these aggregates is shown in the AFM image of Fig. 2c. Here, the rough morphology, with height differences close to 1 μm, is evident. For this reason, we have focused our analysis on the regions relatively free from such structures with the hope of finding smaller GNR flakes or aggregates. One example is displayed in Fig. 2d, where on the GC surface different flat flakes can be distinguished. Their thickness varies in the 20–40 nm range. The presence of these flakes is even more evident in the corresponding phase-contrast image (Fig. 2f) since they yield a quite different contrast than the surrounding GC surface. Moreover, the lateral size of these structures in the phase-contrast image is appreciably larger than that of the corresponding topographical ones. This fact suggests that even thinner GNR flakes must be present, which are difficult to detect topographically due to the rough surface of the underlying GC surface.

Fig. 2e is a 3D view of the flake marked with a rectangle in Fig. 2d. Here, it can be appreciated the extreme flatness and the stepped morphology of the flake. The root mean square roughness of a terrace is close to 0.5 nm. Finally, to assess the different properties of these flakes with respect to the GC substrate, we also performed single pass KFM imaging (see Fig. 2 g-i). Fig. 2g shows a zoom of a GNR flat flake whereas Fig. 2h and i shows the CPD and capacitance gradient images, respectively, taken simultaneously. Clearly, the flake presents higher CPD and lower capacitance gradient signals than the GC surface, which confirms the different electrical properties of the flakes. It is worth noting, as commented above, that the GC surface at this level of resolution displays a sort of granular nanometer structure. One issue to discuss is the nature of the interaction between GNR and GC. These data do show that there are GNR lying parallel to the GC surface. This adsorption geometry suggests that π-π stacking may be ruling the interaction between GNR and GC. In fact, it has recently been stated that the GNR-GC interaction is via π-π stacking [36]. The fact that many carbon atoms are involved in the adsorption is consistent with this type of interaction [37]. In this sense, it is worth noting that the GNR structures remain on the GC surface after repetitive washing of the surface as well as during the sample measurement.

3.1.2. Aryldiazonium electrografting at GC/GNR surface

The next step of the biosensor development consists in modifying the GC/GNR surface with 4-aminobenzoic acid by electrografting of the in-situ generated diazonium cations. In a first step, the diazonium salt is

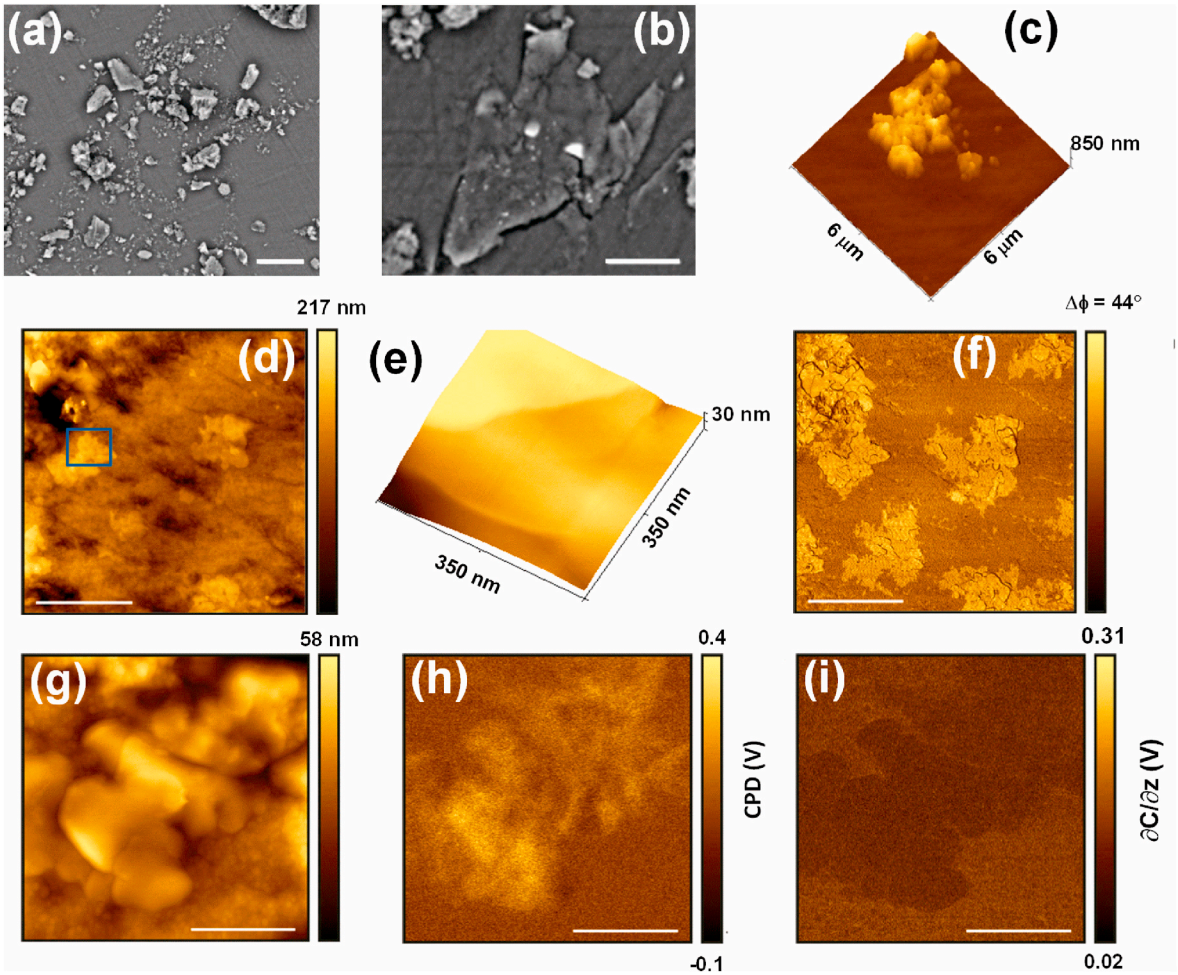

Fig. 2. (a) SEM image of the GC/GNR sample. The bar indicates 10 μm. (b) SEM image of a flat aggregate of the same sample. The bar corresponds to 4 μm. (c) 3D AFM image of one of the rough aggregates found in the GC/GNR surface. (d) AFM image of a flat area of the GC/GNR sample in which several flat GNR flakes are observed. The bar corresponds to 2 μm. (e) 3D AFM image of the flake marked with a rectangle in (d). (f) Phase-contrast image taken simultaneously to the topography of (d). The bar indicates 2 μm. (g) Topographic AFM image of a flake of the GC/GNR sample. The bar corresponds to 500 nm. CPD (h) and ∂C/∂z (i) images taken simultaneously to the topography in (g). The bars indicate 500 nm.

formed from 4-aminobenzoic acid molecules by a standard diazotization procedure. Afterwards, they are electrochemically reduced leading to a covalent bond between carbon atoms of the GNR-modified electrode surface and the benzoic acid. This latter process is achieved through the cyclic voltammograms recorded with a GC/GNR electrode immersed in the solution containing the in-situ generated 4-carboxyphenyl diazonium cations. As Fig. 3a shows, during the first scan, an irreversible peak close to −0.4 V, corresponding to the reduction of diazonium cations to radicals, is obtained. The intensity of this peak decreases with successive scans (see the thick arrow in the figure), indicating that the electrografting is successfully taking place.

Next, we have evaluated by CV (Fig. 3b) the blocking properties of the benzoic acid layer, electrografted after a given number of reduction cycles in a ferri/ferrocyanide solution. The repulsion between the negatively charged carboxylic groups and the $[Fe(CN)_6]^{3-/4-}$ anions hinders the access of the redox probe to the electrode [38], allowing to follow the electrografting process. Fig. 3b shows the typical cyclic voltammogram for $[Fe(CN)_6]^{3-/4-}$, which becomes clearly distorted when the benzoic acid is on the electrode surface. As expected, the increase of the irreversibility and the decrease of the intensity of the peak current are produced as a consequence of the successive electrografting cycles (indicated by the thick arrows in the figure). The higher the number of cycles employed, the higher the extent to which the electron transfer between the redox probe and the electrode surface becomes hindered.

In order to confirm this result, we performed EIS measurements to evaluate the charge transfer process occurring at the electrode interface. Fig. 3c shows Nyquist diagrams in a solution containing $[Fe(CN)_6]^{3-/4-}$ for GC/GNR/BzA where the benzoic acid was electrografted after a given number of cycles (n = 1, 2, 3, 5, 7). As can be observed, the electron-transfer resistance (R_{CT}) increases with the number of cyclic voltammetric scans employed for electrografting.

According to these results, we selected to apply 5 cycles for the reduction of the in-situ generated 4-carboxyphenyl diazonium cations. This number of electro-reduction scans assures that the 4-carboxyphenyl diazonium cations are reduced, as can be seen in Fig. 3a, where the irreversible peak at −0.4 V disappears after the fifth scan.

We have also studied by AFM how the diazonium layer wets the GC substrate by measuring the GC/BzA surface (not shown). This analysis shows how this layer does not affect the overall morphology of the underlying substrate. In addition, the corresponding phase-contrast image obtained simultaneously with the topographical one shows a uniform and homogeneous contrast, which indicates that the diazonium layer fully covers the surface.

In order to estimate the diazonium layer thickness, we first performed a scratching procedure. It consists of sweeping in contact mode a given area during several minutes in order to remove the soft outer layer. Then the image mode is switched to the dynamic mode again and a large area containing the scratched area is imaged with the same tip

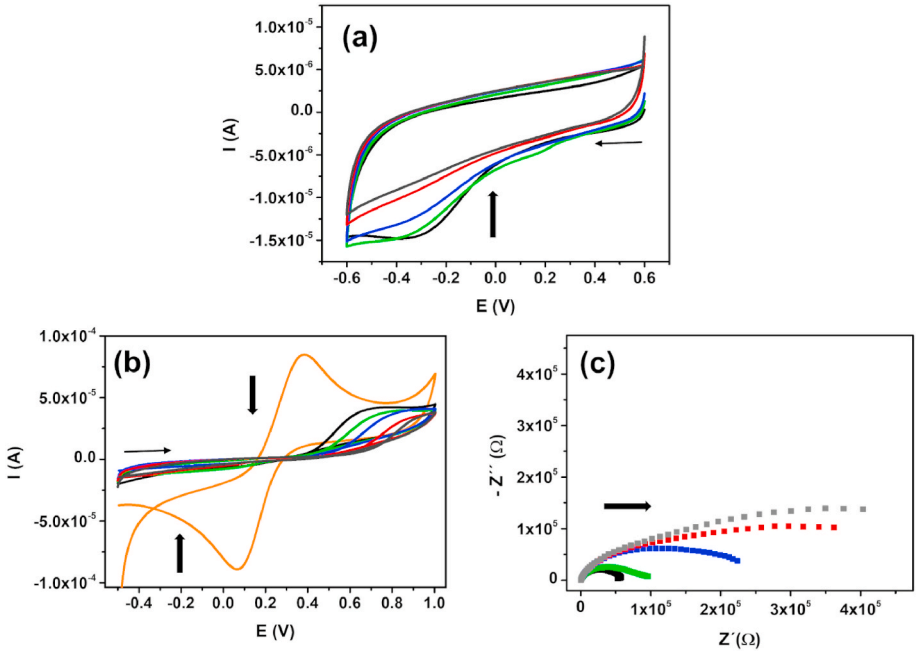

Fig. 3. (a) Successive scans recorded with GC/GNR in a medium containing 4-aminobenzoic acid diazonium salt. For clarity only scans 1 (black line), 2 (green line), 3 (blue line), 5 (red line) and 7 (grey line) are shown. Scan rate 200 mV s^{-1}, E (V) vs Ag/AgCl |1 M KCl. (b) Cyclic voltammograms and (c) Nyquist plots recorded in 0.1 M phosphate buffer pH 7 containing $[Fe(CN)_6]^{3-/4-}$ (1 and 5 mM for CV and EIS, respectively) with GC/GNR/BzA where BzA has been electrografted after 1, 2, 3, 5 and 7 reduction cycles. The response of GC/GNR before the electrografting process is also shown in CV (orange curve in b). Other conditions for CVs in 2b: scan rate 100 mVs^{-1}; E (V) vs Ag/AgCl |1 M KCl. Other conditions for EIS: Measurements at open circuit potential using a sinusoidal voltage of 10 mV amplitude in the frequency range 10^5 Hz-10^{-1} Hz for EIS. The thin arrows indicate the scan direction whereas the thick ones mark the evolution of the measurements with the successive reduction cycles from 1 to 7. (For interpretation of the references to colour in this figure legend, the reader is referred to the Web version of this article.)

(Fig. S1). The change in the phase contrast between the scratched and unscratched areas confirms that the soft BzA layer has been effectively removed. In this way, it can be obtained an estimation of the layer thickness, which results to be close to 9 nm. This value can be an overestimation because some layers of the GC surface can be also removed. However, a more local analysis was done (see below, discussion of Fig. 5d) through force curve analysis that led to a BzA layer thickness close to 4 nm.

Next, we analysed by AFM the morphology of the GC/GNR/BzA system. One example is shown in Fig. 4.

In this image, taken on a relatively rough zone of the glassy substrate, a clear GNR flake zone is observed at the top right part of the image. These flakes display a smooth surface, with a surface roughness of 0.5 nm, which is very similar to that found on the bare flakes. As noted above when discussing the GC/BzA system, the diazonium layer does not appreciably affect the morphology and roughness of the GNR structures under these imaging conditions. However, it is worth to note that the phase-contrast image displays a rather homogeneous contrast, considerably lower than that of Fig. 2f for the bare GNR on GC. This is a consequence of the BzA layer deposited on the whole surface. The fact that still some phase-contrast does exist between the GC/BzA and GNR/BzA structures is due to the imaging conditions as well as to the thinness of the BzA soft organic layer [39].

3.1.3. GC/GNR/BzA/LOx surface

Once the grafting is made, the carboxylic group is activated by adding a solution containing EDC and NHS onto the GC/GNR/BzA surface, before placing it in contact with the enzyme. The biosensing platform, containing all the elements (GC/GNR/BzA/LOx), was visualized by AFM. For this study, the LOx concentration used was considerably lower than that used in the final device in order to be able to locate the smaller GNR flakes. Fig. 5a shows an isolated flake in the bottom half part of the image. The flake has a lateral size of 600 nm and a thickness in the 10–15 nm range. A higher resolution image of the surface of the flake is displayed in Fig. 5b. The vertical scale has been enhanced in order to better show the globular structures found on the top of the flake. The size of these structures is in the 8–14 nm range. Taken into account the extreme flatness of the GNR flakes (see Fig. 2), the globular structures can be ascribed to the LOx molecules. The sizes measured on this flake are slightly larger than those previously imaged under buffer conditions on LOx monolayers [40]. This can be due to the measuring conditions in air. Fig. 5c shows a three-dimensional view of the top of

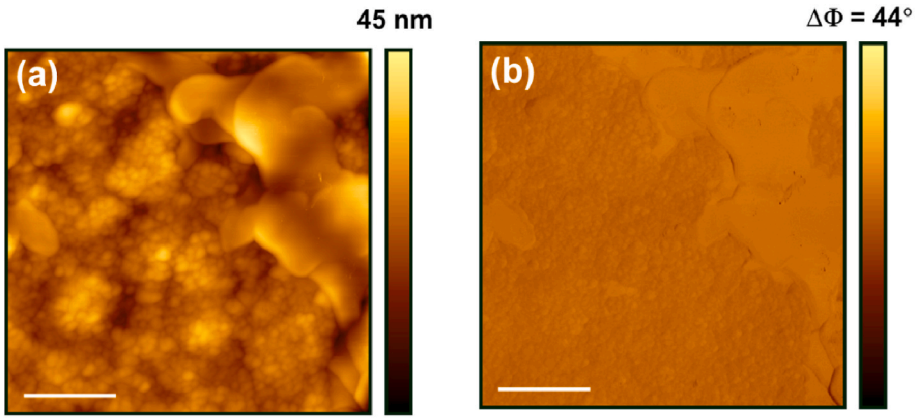

Fig. 4. Topographic (a) and phase-contrast (b) AFM images taken simultaneously in the dynamic mode of the GC/GNR/BzA surface. Note that the vertical scale bar of the phase-contrast image is the same than that of Fig. 2e. The bars indicate 250 nm.

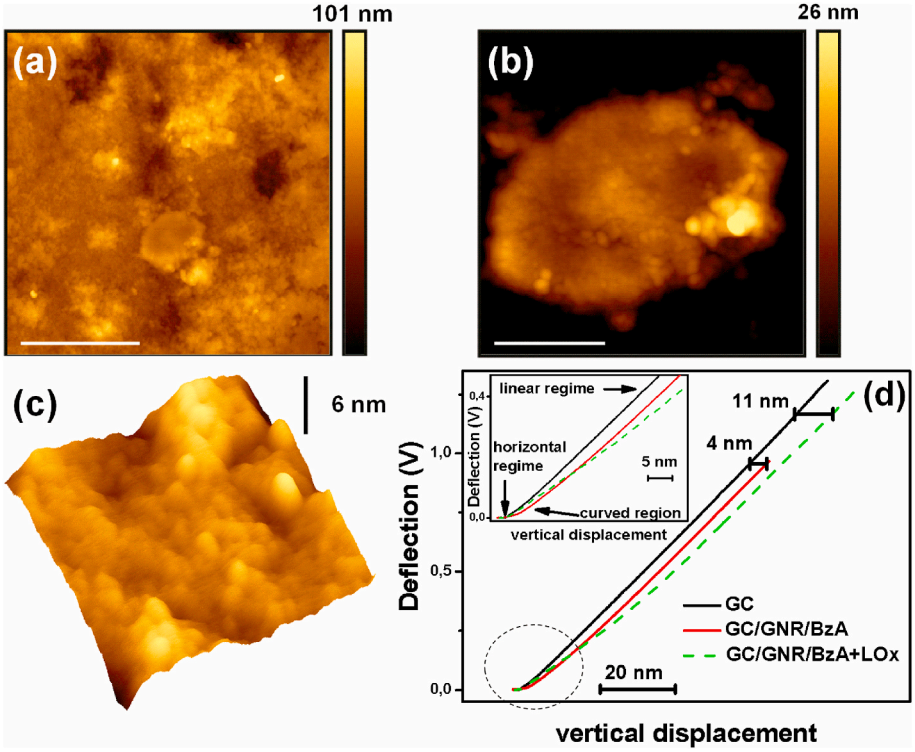

Fig. 5. (a) Topographic AFM image of the GC/GNR/BzA/LOx sample where a flake is observed close to the middle and lying on top of a groove. The bar indicates 1 μm. (b) Zoom of the flake observed in (a) in which the z-scale has been enhanced to make visible the globular structures on its surface. The bar indicates 200 nm. (c) 3D view of the top of the flake of (b). The image is 200 nm × 200 nm wide. (d) Force curves obtained with the same cantilever on the GC (black), GC/GNR/BzA (red) and GC/GNR/BzA/LOx (dashed green) surfaces. The corresponding thickness of the soft layers is indicated. In the top-left inset is plotted a zoom of the graph corresponding to the dashed circle in the main plot. In this inset, the different regions, referred to in the text, are indicated. (For interpretation of the references to colour in this figure legend, the reader is referred to the Web version of this article.)

the flake in order to better appreciate these globular structures. It can be appreciated the rougher surface, compared to that of the bare flakes, as well as the different globular structures. Similar analyses were performed on larger 3D aggregates where globular structures were also imaged (not shown). In these cases, the measured size of the globular structures was higher, probably due to tip convolution effects and the degraded tip condition after measuring such rough 3D agglomerates.

Fig. 5a also suggests that around the GNR flakes, where the morphology is akin to that of the GC substrate, there are also small nanometer rounded structures, which was confirmed by taking higher resolution images (not shown). However, due to nanometer granular morphology of the GC itself, it cannot be confirmed whether these structures are LOx molecules.

In order to further assess this issue, we performed force curve analysis with the same tip on the GC and GC/GNR/BzA surfaces as well as on this surface (Fig. 5d). That one taken on the GC surface mostly shows a horizontal behaviour at the left of the graph followed by a linear dependence with a positive slope (the different regions in the force curve are marked in the inset of Fig. 5d). In contrast, the one obtained on GC/GNR/BzA shows after the horizontal regime a marked curvature before reaching the linear behaviour with the same slope than that observed on the GC surface, the latter regime corresponding to the situation where the tip has gone through the soft layer and has reached the harder underlying surface. Due to the presence of this initial curvature, the force curve is shifted to the right and its lateral extent corresponds to the thickness of the BzA layer [41] that results to be close to 4 nm. This value is in agreement with others reported previously where a sort of multilayer deposition was observed [42–44]. On the GC/GNR/BzA/LOx surface, the force curve presents also a marked curved region, associated to the sampling of soft material, before reaching the constant positive sloped region characteristic of probing the harder GC surface. This initial curved region leads to the shift of the curve respect to that taken on GC, allowing to estimate the thickness of the soft layer around 11 nm. Taking into account that the thickness of the BzA layer is around 4 nm, we can conclude that LOx molecules are indeed adsorbed on the surface, and the LOx layer thickness (around 7 nm) agrees with that of one LOx monolayer [40].

3.2. Response of GC/GNR/BzA/LOx biosensor

In our design of the electrochemical sensor, and keeping in mind the goal of improving the analytical properties of the resulting biosensor towards the determination of lactate, we have focused on the use of GNR in the fabrication of the device and on the adoption of a covalent approach for enzyme immobilization. In the development of biosensing platforms, the immobilization of the enzyme onto the transducer plays a key role in the resulting performance of the device since it is essential that the enzyme retains its full catalytic activity and stability after the immobilization process. In our case, the enzyme (LOx) has been covalently attached to the activated carboxylic groups of the BzA (see Fig. 1), which forces the enzyme to position itself in such a way that it can bind through its amino groups to the activated carboxylic groups exposed from the surface. This could affect its active center and alter its catalytic activity. In order to verify that the enzyme retains its capability for lactate recognition after being immobilized onto the modified electrode, we have recorded the cyclic voltammetric response of the GCE/GNR/BzA/LOx system in a solution containing 1 mM of hydroxymethylferrocene in the absence (Fig. 6, curve a) and in the presence of L-lactate (Fig. 6, curve b).

In the absence of lactate, the typical redox signal around +0.3 V corresponding to the pair redox Fe^{2+}/Fe^{3+} is observed. In the presence of lactate, the CV shows an increase of the anodic peak current together with a decrease of the cathodic one, which is the typical behaviour for catalytic processes involving an enzyme and a redox mediator [45]. The enzymatic reaction proceeds according to the following pathway:

$$\text{L-lactate} + (\text{LOx})_{ox} \rightarrow \text{Pyruvate} + (\text{LOx})_{red} \quad (1)$$

$$(\text{LOx})_{red} + (\text{HMF})_{ox} \rightarrow (\text{LOx})_{ox} + (\text{HMF})_{red} \quad (2)$$

$$(\text{HMF})_{red} \rightarrow (\text{HMF})_{ox} + 1\ e^- \quad (3)$$

In this system, the enzyme LOx catalyzes the oxidation of lactate to pyruvate, while the oxidized form of the soluble redox mediator

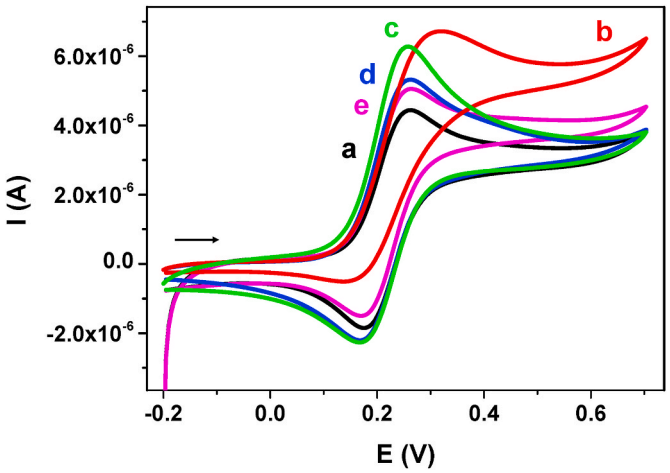

Fig. 6. Cyclic voltammograms in 0.1 M phosphate buffer containing 1 mM HMF recorded with: GC/GNR/BzA/LOx in the absence (curve a) and in the presence (curve b) of 0.4 mM of lactate, GC/GNR/BzA/LOx_{ads} (curve c), GC/BzA/LOx_{ads} (curve d) and GC/BzA/LOx (curve e) in the presence of 0.4 mM of lactate. Other conditions: E (V) vs Ag/AgCl |1 M KCl. Scan rate: 10 mV s^{-1}. The arrow indicates the scan direction.

(HMF_{ox}) accepts the electrons involved in the process, regenerating the enzyme and turning into its reduced form (HMF_{red}). The re-oxidation of HMF_{red} on the electrode surface leads to the response that can be observed in curve b. The magnitude of this catalytic current can be employed as the analytical signal in the determination of lactate concentration. In this detection strategy, HMF replaces O_2 (the natural electron acceptor), allowing to follow its response at +0.3 V, instead of detecting the hydrogen peroxide that is generated when O_2 is employed as electron acceptor. The employment of the redox mediator allows minimizing the contribution of interfering substances that could be oxidized at the high potential required for H_2O_2 detection.

To know whether the covalent approach is more effective than the adsorption of the enzyme in an unspecific way, we have also registered the cyclic voltammetric response towards lactate of the GCE/GNR/BzA/Lox_{ads} biosensor (Fig. 6, curve c). In this case, before adding the enzyme onto the GCE/GNR/BzA surface, we have not performed the activation of the carboxylic groups avoiding the covalent binding. As can be observed in Fig. 6c, in the presence of lactate, the CV shows an increase of the anodic peak current, but this increase is smaller than that obtained in curve b. Furthermore, the cathodic peak current is not reduced, which suggests that the enzyme is working in a less effective way than when it is covalently attached.

On the other hand, as mentioned before, it is known that the use of GNR in the development of electrochemical sensors also influences the final characteristics of the device. In particular, GNR are good candidates for electroanalytical applications due to their properties associated with a great number of rich edge defects and chemically active sites. To evaluate the effect of the GNR on our device, we have recorded the CV response in the presence of lactate when the biosensor does not contain GNR, that is, in which the diazotization step was performed on a bare GC electrode instead of on a GNR-modified one. As can be observed in Fig. 6, the CVs obtained for GC/BzA/LOx_{ads} (curve d) and GC/BzA/LOx (curve e) show an increase of the anodic peak current with respect to that obtained in the absence of lactate, but appreciably smaller than those obtained in curves b and c, reflecting the effect of the absence of GNR. Moreover, the cathodic wave does not show the decrease typically associated to a catalytic behaviour.

3.3. Determination of lactate: analytical data

Fig. 7 shows the calibration curve obtained by plotting the current

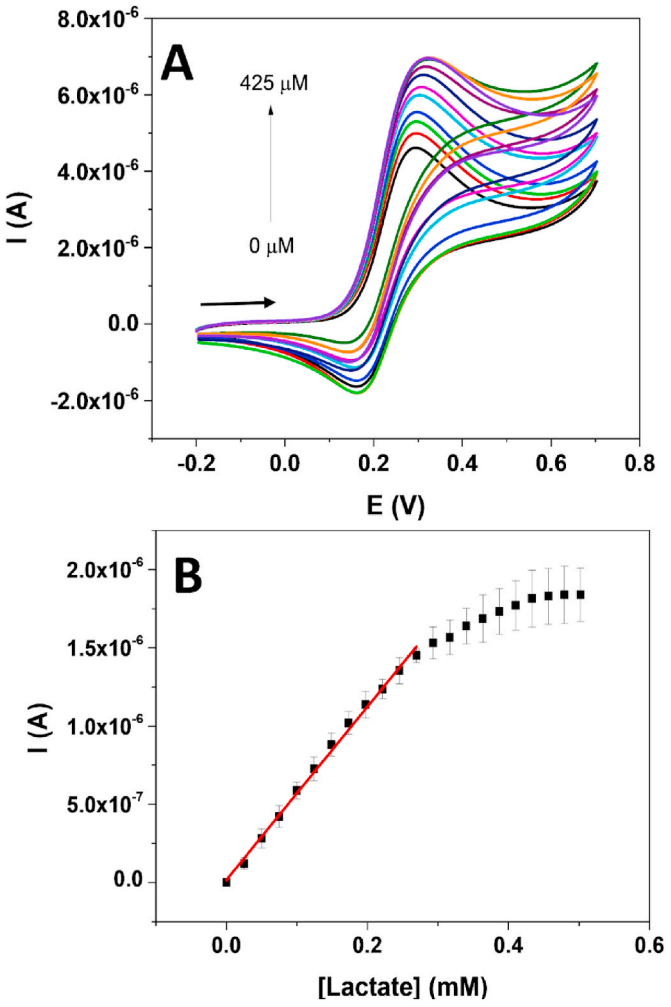

Fig. 7. (a) Cyclic voltammograms recorded in 0.1 M phosphate buffer containing 1 mM of HMF in the presence of increasing lactate concentrations. Other conditions: scan rate: 10 mV s^{-1}; E (V) vs Ag/AgCl | 1 M KCl. The arrow indicates the scan direction. (b) Calibration curve obtained from cyclic voltammetric measurements in (a) (current intensity measured at +0.3 V with respect to the response of HMF in the absence of lactate).

intensity measured at +0.3 V in the cyclic voltammograms recorded with the GC/GNR/BzA/LOx sensor in solutions containing increasing concentration of lactate.

For each concentration value, it is shown the average of the intensity current obtained for three measurements together with the standard deviation (n = 3). In the concentration range of $3.4 \cdot 10^{-5} - 2.8 \cdot 10^{-4}$ M, we obtain a linear relationship whose equation is I (A) = $(1.6 \pm 0.8) \times 10^{-8} + (5.5 \pm 0.1) \times 10^{-6}$ [Lactate] (mM) (r = 0.997). A sensitivity value of 5.5×10^{-6} A/mM was obtained from the slope of the linear range of the calibration curve. Detection (LOD) and determination limits (LOQ) were calculated as 3σ/slope and 10 σ/slope, respectively, where σ corresponds to the standard deviation of the background current (n = 5) and *slope* is the slope (sensitivity) of the linear range of the calibration curve. Values of 11 µM and 34 µM, were found, respectively. We want to highlight that this LOQ is far low enough to control the growth of selected LAB strands in the industrial fermentation of foods and beverages from the beginning of the process until the fermented product is ready [46–49]. For example, specific strains in winemaking gave rise to $(1.8 \pm 0.1)\ 10^{-3}$ M [47], 0.013769 ± 0.000547 M in blueberry juice [46], 0.0850 ± 0.0006 M in the Turkish non-alcoholic beverage Şalgam [48] and as high as 1.15 ± 0.04 M in orange juice milk-based beverages [49].

In order to establish undoubtedly that the best analytical properties are obtained for the GC/GNR/BzA/LOx biosensing platform, we have also obtained the calibration curves for the biosensors that do not include GNR and/or the biosensors where the enzyme was not covalently bonded. Fig. S2 displays the calibration curves for sensors prepared by: direct adsorption of the enzyme on a bare glassy carbon electrode (GC/LOx_{ads}, curve a) and for the GC/GNR/BzA/LOx (curve b), GC/GNR/BzA/LOx_{ads} (curve c), GC/BzA/LOx_{ads} (curve d), GC/BzA/LOx (curve e) systems. The linear concentration range and the sensitivity obtained from the linear part of the calibration curves displayed in Fig. S2 are summarized in Table S1. From these data, it is clearly concluded that the greater sensitivity and the wider linear concentration range are obtained for the GC/GNR/BzA/LOx biosensor. Moreover, the worst results are obtained for biosensors that do not include GNR and in which the enzyme is directly adsorbed onto the electrode surface (GC/LOx_{ads} and GC/BzA/LOx_{ads}), followed by biosensors that do not include GNR but the enzyme is covalently bonded (GC/BzA/LOx). Finally, the linear concentration range and the sensitivity obtained for biosensors containing GNR, but in which the enzyme is adsorbed (GC/GNR/BzA/LOx_{ads}), is worse than those obtained when the enzyme is covalently immobilized.

The accuracy and precision of the method are summarized in Table S2. The accuracy, expressed as relative error (Er,%), has been evaluated by recovery tests performed by triplicate for different level of lactate concentration (0.15 mM, 0.20 mM and 0.25 mM). Er values correspond to the difference between the expected value and the average of the lactate concentration found from the three measurements. The precision of the method was evaluated in terms of reproducibility (measurements performed with different GCE/GNR/BzA/LOx biosensors for different levels of lactate concentrations and inter-day measurements) [50]. For all the concentration levels assayed, relative errors (Er) less than 6.0% and relative standard deviation (RSD) less than 8.4% were calculated, indicating that lactate can be detected with the GC/GNR/BzA/LOx biosensor with good accuracy and precision.

Finally, to evaluate stability, GC/GNR/BzA/LOx biosensors were prepared and kept at 4 °C for 30 days. The biosensor retained 95% of their initial response after the storage period, indicating a good stability.

Table 1 summarizes the analytical properties obtained with different biosensing platforms for lactate determination found in the literature. The detection limit obtained with our biosensing platform is similar, or even better, than those obtained with other recently reported electrochemical biosensors, most of them requiring the combined use of different nanomaterials in their design.

Table 1
Analytical properties of lactate biosensors found in the literature.

Work	Electrode Modification	Linear Concentration Range (mM)	Detection Limit (μM)
[51]	LOx/PtNPs/GCNF/SPCEs	0.01–2.0	6.9
[52]	LOx/AuNPs/ZnO NRs/Au	0.01–0.6	6
[53]	LDH/rGO/AuNPs/SPCEs	0.01–5	0.13
[54]	LDH/rGO-PhNHOH/GC	Up to 0.090	2.5
[55]	MWCNTs/CS/LOx/SPBGE	0.03–0.24	22.6
[4]	FTFME/b-Cyt/engineered LOx	0.5–20	410
[5]	g-p MgO-tC-SP/NTQ/LOx	Up to 50	300
[6]	Pd electrode/Flex-GO/LOx	1–100	1000
[7]	SPCEs/PtNPs/PANI/MXene/LOx	0.005–5	5
[8]	Pt/rGO/CNTs/AuNPs/LOx	0.05–100	2.3
[9]	Au SGGT/PC/CeO_2NPs/LOx	0.003–0.3	0.3
[10]	Ni foam/TiO_2/graphene/LOx	0.05–10	19
[41]	Au/DNPs/LOx	0.05–0.7	15
[56]	Au/MPTS/DNPs/LOx	0.053–1.6	16
[57]	GC/MoS_2/LOx	0.056–0.77	17
This work	GCE/GNR/BzA/LOx	0.035–0.28	11

Lactate oxidase (LOx), platinum nanoparticles (PtNPs), graphitized carbon nanofibers (GCNF), screen printed carbon electrodes (SPCEs), gold nanoparticles (AuNPs), zinc oxide nanorods (ZnO NRs), Lactate dehydrogenase (LDH), reduced graphene oxide (rGO), glassy carbon electrode (GC), multiwalled carbon nanotubes (MWCNTs), chitosan (CS), basal-plane like screen-printed graphite electrodes (SPBGEs), flexible thin-film multiplexed electrodes (FTFME), b-type cytochrome protein (b-Cyt), screen-printed graft-polymerized MgO-templated carbon (g-p MgO-tC-SP), 1,2-naphthoquinone (NTQ), Flex-GO (Flexible graphene oxide), polyaniline (PANI), transition metal carbide and nitride (MXene), carbon nanotubes (CNTs), solution-gated graphene transistors based on Au (Au SGGT), porous carbon (PC), diamond nanoparticles (DNPs), (3-mercaptopropyl)-trimethoxysilane (MPTS), chevron-like graphene nanoribbons (GNR), 4-aminobenzoic acid (BzA).

3.4. Interference study

In order to evaluate the selectivity of the method, glucose, fructose, ascorbic acid, tartaric acid and citric acid were studied as potential interferences in lactate determination since these compounds are typically present in juices. The study was performed by recording the GC/GNR/BzA/LOx biosensor response before and after adding increasing amounts of each potential interferent to a solution containing a fixed amount of lactate ($1.5\ 10^{-4}$ M). According to the criteria that a given compound interferes at a concentration level enough to produce a variation on the initial analytical signal higher than 10%, we found that the presence of glucose, fructose, ascorbic acid, tartaric acid and citric acid interferes for the concentrations summarized in Table S3.

3.5. Analytical application: determination of lactate in juices

The applicability of the sensor was evaluated for lactate determination in apple juices because this sample is a target of the food industry and there is a need for controlling the growth (so the fermentation) of LAB. As described in the experimental section, only filtration was carried out, as pretreatment of the juice sample, before performing the analysis by standard addition procedure. To this end, different aliquots of 250 μL of apple juice were mixed with increasing volumes of a standard solution of lactate before made up all of them to a final volume of 5.00 mL in volumetric flasks, employing 0.1 M phosphate buffer (pH 7) containing 1.0 mM hydroxymethylferrocene. In addition, one solution containing only the aliquot of 250 μL of sample, without addition of lactate, was prepared in the same way. This corresponds to $[Lactate]_{added} = 0$. From cyclic voltammetric measurements (Fig. S3), it was found that the current increases with lactate addition according to $I\ (A) = (6.3 \pm 0.5)\ x\ 10^{-7} + (7.9 \pm 0.2)\ x\ 10^{-6}\ [Lactate]_{added}$ (mM), $r = 0.992$. The sample concentration was obtained by extrapolation of this straight line to $y = 0$. From this value, and after taking into account the dilution of the sample (1:20), a lactate concentration of 1.59 ± 0.07 mM in the apple juice was found. The assays were carried out in triplicate.

To validate the result obtained by the electrochemical-based methodology, the apple juice samples were further analysed with a commercial enzymatic lactate assay kit according to the manufacturer's instructions (Neogen). The measurement is based on the spectrophotometric determination at 340 nm of the nicotinamide adenine dinucleotide formed from lactate through two coupled reactions catalyzed by L-lactate dehydrogenase and glutamate-pyruvate transaminase. A lactate concentration of 1.55 ± 0.07 mM ($n = 3$) was obtained. In order to compare statistically the results obtained by both electrochemical and spectrophotometric measurements, we applied the Student *t*-test, obtaining a t_{cal} value ($t_{cal} = 0.70$) lower than the tabulated one ($t_{tab} =$

4.60 for 99%). This data indicates that results obtained by both methods are in very good agreement, confirming the applicability of the proposed methodology for lactate determination in beverages, even when the sample was not subjected to fermentation by LAB, i.e., with the raw liquid.

4. Conclusions

We have developed an electrochemical biosensor for lactic acid determination based on the covalent immobilization of lactate oxidase via a diazotation process onto a glassy carbon electrode modified with bottom-up synthesized chevron-like graphene nanoribbons. The diazonium salt, formed from 4-aminobenzoic acid molecules, was successfully anchored to the GNR-modified electrode surface by electrochemical reduction after applying 5 cyclic voltammetric scans. The characterization of the biosensing surface by AFM shows flakes, with lateral size around 600 nm and a thickness in the 10–15 nm range, decorated with globular structures in the 8–14 nm range ascribed to the LOx enzyme. Force curve analysis allows to estimate the thickness of the soft layer around 11 nm, which is formed by BzA and LOx layers of around 4 and 7 nm, respectively.

The biosensing platform, including GNR and a covalent approach for the immobilization of the enzyme, shows a higher electrocatalytic response towards lactate than similar biosensors that do not include GNR and/or where the enzyme was adsorbed in an unspecific way, evidencing that the biosensor design combines the benefits in selectivity provided by the enzyme with the sensitivity derived from the use of GNR.

The biosensor responds linearly to lactate in the range $3.4 \cdot 10^{-5}$– $2.8 \cdot 10^{-4}$ M with a limit of detection of 11 μM and its applicability to determine lactate in apple juices has been tested with results in good agreement with those obtained by an enzymatic-spectrophotometric assay kit.

CRediT authorship contribution statement

Raquel Sainz: Investigation, Validation, Writing – review & editing. **María del Pozo:** Investigation, Validation, Visualization, Writing – review & editing. **Luis Vázquez:** Methodology, Investigation, Visualization, Writing – original draft, Writing – review & editing. **Manuel Vilas-Varela:** Investigation, Writing – review & editing. **Jesús Castro-Esteban:** Investigation, Writing – review & editing. **Elías Blanco:** Visualization, Writing – review & editing. **María Dolores Petit-Domínguez:** Conceptualization, Methodology, Supervision, Writing – review & editing, Project administration, Funding acquisition. **Carmen Quintana:** Conceptualization, Methodology, Supervision, Writing – review & editing, Project administration, Funding acquisition. **Elena Casero:** Conceptualization, Methodology, Supervision, Writing – original draft, Writing – review & editing, Project administration, Funding acquisition.

Declaration of competing interest

The authors declare that they have no known competing financial interests or personal relationships that could have appeared to influence the work reported in this paper.

Acknowledgements

The authors acknowledge financial support from the European Union's Horizon 2020 research and innovation programme (Project SPRING, grant agreement No 863098), the European Research Council (ERC) (Project MolDAM, grant agreement No 951519), Ministerio de Ciencia e Innovación of Spain (Grants MAT2017-85089-C2-1-R, MAT2017-85089-C2-2-R, PID2020-113142RB-C21, PID2020-113142RB-C22) funded by MCIN/AEI/10.13039/501100011033, the Comunidad Autónoma de Madrid (S2018/NMT-4349 TRANSNANOAVANSENS-CM), the Xunta de Galicia (Centro singular de investigación de Galicia accreditation 2019–2022, ED431G 2019/03) and the European Union (European Regional Development Fund - ERDF). J. Castro thanks the Spanish MINECO and the European Social Fund for the predoctoral grant BES-2017-081094. We want to thank Ismael Ballesteros for the SEM measurements.

Appendix A. Supplementary data

Supplementary data to this article can be found online at https://doi.org/10.1016/j.aca.2022.339851.

References

[1] F. Leroy, L. De Vuyst, Lactic acid bacteria as functional starter cultures for the food fermentation industry, Trends Food Sci. Technol. 15 (2004) 67–78, https://doi.org/10.1016/j.tifs.2003.09.004.
[2] R. Di Cagno, R. Coda, M. De Angelis, M. Gobbetti, Exploitation of vegetables and fruits through lactic acid fermentation, Food Microbiol. 33 (2013) 1–10, https://doi.org/10.1016/j.fm.2012.09.003.
[3] A. Septembre-Malaterre, F. Remize, P. Poucheret, Fruits and vegetables, as a source of nutritional compounds and phytochemicals: changes in bioactive compounds during lactic fermentation, Food Res. Int. 104 (2018) 86–99, https://doi.org/10.1016/j.foodres.2017.09.031.
[4] K. Hiraka, W. Tsugawa, R. Asano, M.A. Yokus, K. Ikebukuro, M.A. Daniele, K. Sode, Rational design of direct electron transfer type L-lactate dehydrogenase for the development of multiplexed biosensor, Biosens. Bioelectron. 176 (2021) 112933, https://doi.org/10.1016/j.bios.2020.112933.
[5] I. Shitanda, M. Mitsumoto, N. Loew, Y. Yoshihara, H. Watanabe, T. Mikawa, S. Tsujimura, M. Itagaki, M. Motosuke, Continuous sweat lactate monitoring system with integrated screen-printed MgO-templated carbon-lactate oxidase biosensor and microfluidic sweat collector, Electrochim. Acta 368 (2021) 137620, https://doi.org/10.1016/j.electacta.2020.137620.
[6] K.C. Lin, S. Muthukumar, S. Prasad, Flex-GO (Flexible graphene oxide) sensor for electrochemical monitoring lactate in low-volume passive perspired human sweat, Talanta 214 (2020) 120810, https://doi.org/10.1016/j.talanta.2020.120810.
[7] S. Neampet, N. Ruecha, J. Qin, W. Wonsawat, O. Chailapakul, N. Rodthongkum, A nanocomposite prepared from platinum particles, polyaniline and a Ti3C2 MXene for amperometric sensing of hydrogen peroxide and lactate, Microchim. Acta 186 (2019) 752, https://doi.org/10.1007/s00604-019-3845-3.
[8] S. Hashemzadeh, Y. Omidi, H. Rafii-Tabar, Amperometric lactate nanobiosensor based on reduced graphene oxide, carbon nanotube and gold nanoparticle nanocomposite, Microchim. Acta 186 (2019) 680, https://doi.org/10.1007/s00604-019-3791-0.
[9] Y. Bi, L. Ye, Y. Mao, L. Wang, H. Qu, J. Liu, L. Zheng, Porous carbon supported nanoceria derived from one step in situ pyrolysis of Jerusalem artichoke stalk for functionalization of solution-gated graphene transistors for real-time detection of lactic acid from cancer cell metabolism, Biosens. Bioelectron. 140 (2019) 111271, https://doi.org/10.1016/j.bios.2019.04.039.
[10] S. Boobphahom, P. Rattanawaleedirojn, Y. Boonyongmaneerat, S. Rengpipat, O. Chailapakul, N. Rodthongkum, TiO_2 sol/graphene modified 3D porous Ni foam: a novel platform for enzymatic electrochemical biosensor, J. Electroanal. Chem. 833 (2019) 133–142, https://doi.org/10.1016/j.jelechem.2018.11.031.
[11] J.V. Piovesan, E.R. Santana, A. Spinelli, A carbon paste electrode improved with poly(ethylene glycol) for tannic acid surveillance in beer samples, Food Chem. 326 (2020) 127055, https://doi.org/10.1016/j.foodchem.2020.127055.
[12] E.R. Santana, A. Spinelli, Electrode modified with graphene quantum dots supported in chitosan for electrochemical methods and non-linear deconvolution of spectra for spectrometric methods: approaches for simultaneous determination of triclosan and methylparaben, Microchim. Acta 187 (2020) 250, https://doi.org/10.1007/s00604-020-04225-7.
[13] I.S. Kucherenko, O.O. Soldatkin, D.Y. Kucherenko, O.V. Soldatkina, S. V. Dzyadevych, Advances in nanomaterial application in enzyme-based electrochemical biosensors: a review, Nanoscale Adv. 1 (2019) 4560–4577, https://doi.org/10.1039/c9na00491b.
[14] L. Zhang, Y. Ying, Y. Li, Y. Fu, Integration and synergy in protein-nanomaterial hybrids for biosensing: strategies and in-field detection applications, Biosens. Bioelectron. 154 (2020) 112036, https://doi.org/10.1016/j.bios.2020.112036.
[15] X. Wang, F. Li, Y. Guo, Recent trends in nanomaterial-based biosensors for point-of-care testing, Front. Chem. 8 (2020) 586702, https://doi.org/10.3389/fchem.2020.586702.
[16] R. Sainz, M. Del Pozo, M. Vilas-Varela, J. Castro-Esteban, M. Perez Corral, L. Vazquez, E. Blanco, D. Pena, J.A. Martin-Gago, G.J. Ellis, M.D. Petit-Dominguez, C. Quintana, E. Casero, Chemically synthesized chevron-like graphene nanoribbons for electrochemical sensors development: determination of epinephrine, Sci. Rep. 10 (2020) 14614, https://doi.org/10.1038/s41598-020-71554-1.
[17] Z. Xiao, L. Sheng, L. Jiang, Y. Zhao, M. Jiang, X. Zhang, M. Zhang, J. Shi, Y. Lin, Z. Fan, Nitrogen-doped graphene ribbons/MoS_2 with ultrafast electron and ion transport for high-rate Li-ion batteries, Chem. Eng. J. 408 (2021), 127269, https://doi.org/10.1016/j.cej.2020.127269.

[18] Y. Zhu, A.L. Higginbotham, J.M. Tour, Covalent functionalization of surfactant-wrapped graphene nanoribbons, Chem. Mater. 21 (2009) 5284–5291, https://doi.org/10.1021/cm902939n.
[19] Z. Ding, J. Liang, W. Zhang, W. Wang, R. Geng, Y. Wang, P. Li, Q. Fan, Efficiency and active sites of the synergetic sorption and photocatalysis in Cr(VI) decontamination on a 3D oxidized graphene ribbon framework, J. Mater. Chem. A. 8 (2020) 11362–11369, https://doi.org/10.1039/d0ta01847c.
[20] H. Latif, D. Wasif, S. Rasheed, A. Sattar, M.S. Rafique, A.W. Anwar, S. Zaheer, S. A. Shabbir, A. Imtiaz, M. Qutab, A. Usman, Gold nanoparticles mixed multiwall carbon nanotubes, supported on graphene nano-ribbons (Au-NT-G) as an efficient reduction electrode for polymer electrolyte membrane fuel cells (PEMFC), Renew. Energy 154 (2020) 767–773, https://doi.org/10.1016/j.renene.2020.03.061.
[21] A.P. Johnson, C. Sabu, N.K. Swamy, A. Anto, H.V. Gangadharappa, K. Pramod, Graphene nanoribbon: an emerging and efficient flat molecular platform for advanced biosensing, Biosens. Bioelectron. 184 (2021) 113245, https://doi.org/10.1016/j.bios.2021.113245.
[22] S. Đurđić, V. Vukojević, F. Vlahović, M. Ognjanović, L. Svorc, K. Kalcher, J. Mutić, D.M. Stanković, Application of bismuth (III) oxide decorated graphene nanoribbons for enzymatic glucose biosensing, J. Electroanal. Chem. 850 (2019) 113400, https://doi.org/10.1016/j.jelechem.2019.113400.
[23] S. Sandeep, A.S. Santhosh, N.K. Swamy, G.S. Suresh, J.S. Melo, N.A. Chamaraja, A biosensor based on a graphene nanoribbon/silver nanoparticle/polyphenol oxidase composite matrix on a graphite electrode: application in the analysis of catechol in green tea samples, New J. Chem. 42 (2018) 16620–16629, https://doi.org/10.1039/C8NJ02325E.
[24] V. Mani, M. Govindasamy, S.M. Chen, T.W. Chen, A.S. Kumar, S.T. Huang, Core-shell heterostructured multiwalled carbon nanotubes@reduced graphene oxide nanoribbons/chitosan, a robust nanobiocomposite for enzymatic biosensing of hydrogen peroxide and nitrite, Sci. Rep. 7 (2017) 11910, https://doi.org/10.1038/s41598-017-12050-x.
[25] V. Vukojević, S. Djurdjić, M. Ognjanović, M. Fabián, A. Samphao, K. Kalcher, D. M. Stanković, Enzymatic glucose biosensor based on manganese dioxide nanoparticles decorated on graphene nanoribbons, J. Electroanal. Chem. 823 (2018) 610–616, https://doi.org/10.1016/j.jelechem.2018.07.013.
[26] E. Mehmeti, D.M. Stanković, S. Chaiyo, J. Zavasnik, K. Žagar, K. Kalcher, Wiring of glucose oxidase with graphene nanoribbons: an electrochemical third generation glucose biosensor, Microchim. Acta 184 (2017) 1127–1134, https://doi.org/10.1007/s00604-017-2115-5.
[27] J. Qian, X. Yang, Z. Yang, G. Zhu, H. Mao, K. Wang, Multiwalled carbon nanotube@reduced graphene oxide nanoribbon heterostructure: synthesis, intrinsic peroxidase-like catalytic activity, and its application in colorimetric biosensing, J. Mater. Chem. B. 3 (2015) 1624–1632, https://doi.org/10.1039/c4tb01702a.
[28] G.L.C. Paulus, Q.H. Wang, M.S. Strano, Covalent electron transfer chemistry of graphene with diazonium salts, Acc. Chem. Res. 46 (2013) 160–170, https://doi.org/10.1021/ar300119z.
[29] J.L. Bahr, J. Yang, D.V. Kosynkin, M.J. Bronikowski, R.E. Smalley, J.M. Tour, Functionalization of carbon nanotubes by electrochemical reduction of aryl diazonium salts: a bucky paper electrode, J. Am. Chem. Soc. 123 (2001) 6536–6542, https://doi.org/10.1021/ja010462s.
[30] B. Genorio, A. Znidarsic, Functionalization of graphene nanoribbons, J. Phys. D Appl. Phys. 47 (2014), 094012, https://doi.org/10.1088/0022-3727/47/9/094012.
[31] L. Pilan, Tailoring the performance of electrochemical biosensors based on carbon nanomaterials via aryldiazonium electrografting, Bioelectrochemistry 138 (2021) 107697, https://doi.org/10.1016/j.bioelechem.2020.107697.
[32] L. Daukiya, J. Teyssandier, S. Eyley, S. El Kazzi, M.C. Rodríguez González, B. Pradhan, W. Thielemans, J. Hofkens, S. De Feyter, Covalent functionalization of molybdenum disulfide by chemically activated diazonium salts, Nanoscale 13 (2021) 2972–2981, https://doi.org/10.1039/d0nr07310e.
[33] S. Mahouche-Chergui, S. Gam-Derouich, C. Mangeney, M.M. Chehimi, Aryl diazonium salts: a new class of coupling agents for bonding polymers, biomacromolecules and nanoparticles to surfaces, Chem. Soc. Rev. 40 (2011) 4143–4166, https://doi.org/10.1039/c0cs00179a.
[34] M.J. Cadena, R. Misiego, K.C. Smith, A. Avila, B. Pipes, R. Reifenberger, A. Raman, Sub-surface imaging of carbon nanotube-polymer composites using dynamic AFM methods, Nanotechnology 24 (2013) 135706, https://doi.org/10.1088/0957-4484/24/13/135706.
[35] T.H. Vo, M. Shekhirev, D.A. Kunkel, M.D. Morton, E. Berglund, L. Kong, P. M. Wilson, P.A. Dowben, A. Enders, A. Sinitskii, Large-scale solution synthesis of narrow graphene nanoribbons, Nat. Commun. 5 (2014) 3189, https://doi.org/10.1038/ncomms4189.
[36] M.R. Zoric, E.J. Askins, X. Qiao, K.D. Glusac, Strong electronic coupling of graphene nanoribbons onto basal plane of a glassy carbon electrode, ACS Appl. Electron. Mater. 3 (2021) 854–860, https://doi.org/10.1021/acsaelm.0c00978.
[37] S. Grimme, Do special noncovalent p–p stacking interactions really exist? Angew. Chem. Int. Ed. 47 (2008) 3430–3434, https://doi.org/10.1002/anie.200705157.
[38] A. Hayat, L. Barthelmebs, A. Sassolas, J.L. Marty, An electrochemical immunosensor based on covalent immobilization of okadaic acid onto screen printed carbon electrode via diazotization-coupling reaction, Talanta 85 (2011) 513–518, https://doi.org/10.1016/j.talanta.2011.04.034.
[39] H. Li, L. Sun, G. Shen, Q. Liang, The nanoscale phase distinguishing of PCL-PB-PCL blended in epoxy resin by tapping mode atomic force microscopy, Nanoscale Res. Lett. 7 (2012) 153, https://doi.org/10.1186/1556-276X-7-153.
[40] A. Parra, E. Casero, L. Vázquez, F. Pariente, E. Lorenzo, Design and characterization of a lactate biosensor based on immobilized lactate oxidase onto gold surfaces, Anal. Chim. Acta 555 (2006) 308–315, https://doi.org/10.1016/j.aca.2005.09.025.
[41] M. Briones, E. Casero, M.D. Petit-Domínguez, M.A. Ruiz, A.M. Parra-Alfambra, F. Pariente, E. Lorenzo, L. Vázquez, Diamond nanoparticles based biosensors for efficient glucose and lactate determination, Biosens. Bioelectron. 68 (2015) 521–528, https://doi.org/10.1016/j.bios.2015.01.044.
[42] P.A. Brooksby, A.J. Downard, Electrochemical and atomic force microscopy study of carbon surface modification via diazonium reduction in aqueous and acetonitrile solutions, Langmuir 20 (2004) 5038–5045, https://doi.org/10.1021/la049616i.
[43] J. Greenwood, T.H. Phan, Y. Fujita, Z. Li, O. Ivasenko, W. Vanderlinden, H. Van Gorp, W. Frederickx, G. Lu, K. Tahara, Y. Tobe, H. Uji-I, S.F.L. Mertens, S. De Feyter, Covalent modification of graphene and graphite using diazonium chemistry: tunable grafting and nanomanipulation, ACS Nano 9 (2015) 5520–5535, https://doi.org/10.1021/acsnano.5b01580.
[44] M.C.R. González, P. Carro, L. Vázquez, A.H. Creus, Mapping nanometric electronic property changes induced by an aryl diazonium sub-monolayer on Hopg, Phys. Chem. Chem. Phys. 18 (2016) 29218–29225, https://doi.org/10.1039/c6cp05910d.
[45] N. Loew, T. Ofuji, I. Shitanda, Y. Hoshi, Y. Kitazumi, K. Kano, M. Itagaki, Cyclic voltammetry and electrochemical impedance simulations of the mediator-type enzyme electrode reaction using finite element method, Electrochim. Acta 367 (2021) 137483, https://doi.org/10.1016/j.electacta.2020.137483.
[46] Y. Wu, S. Li, Y. Tao, D. Li, Y. Han, P.L. Show, G. Wen, J. Zhou, Fermentation of blueberry and blackberry juices using Lactobacillus plantarum, Streptococcus thermophilus and Bifidobacterium bifidum: growth of probiotics, metabolism of phenolics, antioxidant capacity in vitro and sensory evaluation, Food Chem. 348 (2021) 129083, https://doi.org/10.1016/j.foodchem.2021.129083.
[47] S. Fairbairn, L. Engelbrecht, M.E. Setati, M. du Toit, F.F. Bauer, B. Divol, D. Rossouw, Combinatorial analysis of population dynamics, metabolite levels and malolactic fermentation in Saccharomyces cerevisiae/Lachancea thermotolerans mixed fermentations, Food Microbiol. 96 (2021) 103712, https://doi.org/10.1016/j.fm.2020.103712.
[48] B. Agirman, L. Settanni, H. Erten, Effect of different mineral salt mixtures and dough extraction procedure on the physical, chemical and microbiological composition of Şalgam: a black carrot fermented beverage, Food Chem. 344 (2021) 128618, https://doi.org/10.1016/j.foodchem.2020.128618.
[49] B. de la Fuente, C. Luz, C. Puchol, G. Meca, F.J. Barba, Evaluation of fermentation assisted by Lactobacillus brevis POM, and Lactobacillus plantarum (TR-7, TR-71, TR-14) on antioxidant compounds and organic acids of an orange juice-milk based beverage, Food Chem. 343 (2021) 128414, https://doi.org/10.1016/j.foodchem.2020.128414.
[50] M. Gumustas, S.A. Ozkan, The role of and the place of method validation in drug analysis using electroanalytical techniques, Open Anal. Chem. J. 5 (2011) 1–21, https://doi.org/10.2174/1874065001005010001.
[51] O.A. Loaiza, P.J. Lamas-Ardisana, L. Añorga, E. Jubete, V. Ruiz, M. Borghei, G. Cabañero, H.J. Grande, Graphitized carbon nanofiber-Pt nanoparticle hybrids as sensitive tool for preparation of screen printing biosensors. Detection of lactate in wines and ciders, Bioelectrochemistry 101 (2015) 58–65, https://doi.org/10.1016/j.bioelechem.2014.07.005.
[52] Y. Zhao, X. Fang, Y. Gu, X. Yan, Z. Kang, X. Zheng, P. Lin, L. Zhao, Y. Zhang, Gold nanoparticles coated zinc oxide nanorods as the matrix for enhanced L-lactate sensing, Colloids Surf. B Biointerfaces 126 (2015) 476–480, https://doi.org/10.1016/j.colsurfb.2014.12.053.
[53] S. Azzouzi, L. Rotariu, A.M. Benito, W.K. Maser, M. Ben Ali, C. Bala, A novel amperometric biosensor based on gold nanoparticles anchored on reduced graphene oxide for sensitive detection of L-lactate tumor biomarker, Biosens. Bioelectron. 69 (2015) 280–286, https://doi.org/10.1016/j.bios.2015.03.012.
[54] B. Manna, C. Retna Raj, Covalent functionalization and electrochemical tuning of reduced graphene oxide for the bioelectrocatalytic sensing of serum lactate, J. Mater. Chem. B. 4 (2016) 4585–4593, https://doi.org/10.1039/c6tb00721j.
[55] N. Hernández-Ibáñez, L. García-Cruz, V. Montiel, C.W. Foster, C.E. Banks, J. Iniesta, Electrochemical lactate biosensor based upon chitosan/carbon nanotubes modified screen-printed graphite electrodes for the determination of lactate in embryonic cell cultures, Biosens. Bioelectron. 77 (2016) 1168–1174, https://doi.org/10.1016/j.bios.2015.11.005.
[56] M. Briones, E. Casero, L. Vázquez, F. Pariente, E. Lorenzo, M.D. Petit-Domínguez, Diamond nanoparticles as a way to improve electron transfer in sol-gel L-lactate biosensing platforms, Anal. Chim. Acta 908 (2016) 141–149, https://doi.org/10.1016/j.aca.2015.12.029.
[57] A.M. Parra-Alfambra, E. Casero, L. Vázquez, C. Quintana, M. del Pozo, M.D. Petit-Domínguez, MoS_2 nanosheets for improving analytical performance of lactate biosensors, Sensor. Actuator. B Chem. 274 (2018) 310–317, https://doi.org/10.1016/j.snb.2018.07.124.